





Josephson current controlled by Fermi-arc surface states of Weyl semimetalsXing Wang , Kai-Yi Lyu , Juntao Song , and Yu-Xian Li **College of Physics and Hebei Advanced Thin Films Laboratory, Hebei Normal University, Shijiazhuang, Hebei 050024, China*

(Received 8 April 2024; revised 11 June 2024; accepted 12 June 2024; published 27 June 2024)

In this paper, the supercurrent of the superconductor (SC)–Weyl semimetal–SC Josephson junction hybrid system is studied based on the Landauer–Büttiker formula combined with the nonequilibrium Green’s method. According to the different edge states, the Fermi arcs are divided into three regions: the symmetric, topological, and insulated regions, which are defined by the azimuthal angle θ and the transverse momentum k_z . Here, θ is the azimuthal angle between the symmetry axis of the Fermi arcs and the normal of the Josephson junction. It is found that the supercurrent is suppressed in the symmetric region. In the topological region, the supercurrent increases with increasing θ . The supercurrent is almost zero in the insulated region due to the presence of the energy gap. The total supercurrent summed over all k_z channels increases and then decreases with increasing θ , that is, θ can control the value of the supercurrent. In addition, the magnetic field and the azimuthal angle θ can adjust the phase transition of the Josephson junction, allowing it to be a 0 , π , or φ_0 junction. These properties provide research ideas for controlling the value of the supercurrent and the Josephson junction phase transition and play an important role in the development and application of superconducting electronic devices.

DOI: [10.1103/PhysRevB.109.235435](https://doi.org/10.1103/PhysRevB.109.235435)**I. INTRODUCTION**

There has been great progress in the study of topological materials, such as topological insulators [1–3]. In recent years, it has been discovered that metals can be topologically classified in addition to insulators. Topological metals have special energy band intersections (nodes). A special class of topological semimetals is given when these nodes are on the Fermi surface. According to the degeneracy of nodes, topological semimetals can be divided into Dirac [4,5], Weyl [6–12], and nodal-line semimetals [13,14]. The Weyl points always appear in pairs with opposite chirality in the absence of time-reversal or inversion symmetry [6,15], and the Fermi arc (FA) spans between each pair of Weyl points in the surface Brillouin zone [8]. Such disconnected FAs can not be realized in any noninteracting two-dimensional (2D) bulk states, and their emergence can serve as the hallmark of Weyl semimetals (WSMs) [10,11,16–19]. Therefore, detecting and manipulating the unique FA surface states of WSMs has attracted a lot of interest from researchers.

Josephson predicted that supercurrent could tunnel in a Josephson junction, which is a sandwich structure of two superconductors (SCs) separated by a thin insulating barrier [20,21]. Anderson and Rowell [22] experimentally confirmed this theory, and this effect was named the Josephson effect. It is well known that Andreev reflection occurs in the ordinary normal metal–SC junctions, and incident electrons with spin \uparrow (\downarrow) reflect holes with spin \downarrow (\uparrow) [23]. When the insulating barrier is replaced by a normal metal or semiconductor, the electrons and holes in the normal region are coherently

coupled to each other by the Andreev reflections at the normal-SC interfaces [23]. The Andreev bound states with discrete energy levels (Andreev levels) are formed in the normal region near the Fermi level within the superconducting energy gap [24,25], which support the transport of Cooper pairs between the left and right SCs and then generate supercurrent [26]. In general, the Josephson free energy is minimum when the superconducting phase difference is zero, and such a Josephson junction is called a 0 junction. When the minimum Josephson free energy appears at a superconducting phase difference of π , such as in the case of a SC-ferromagnet-SC junction [27], this Josephson junction is called a π junction. The transition of a Josephson junction from the 0 (π) state to the π (0) state is referred to as the 0 - π transition, which is mostly achieved by changing the size of the ferromagnet, the relative orientation of magnetizations, and the structural geometry [28–34]. In addition, the Josephson free energy that has only one minimum at the superconducting phase difference of φ_0 is called a φ_0 junction. It was discussed with the nanowire-based Josephson junction applied by the Rashba spin-orbit coupling and the Zeeman field [35–37], the SC-ferromagnet hybrid structures [38], and the magnetized topological insulator interfaces [39]. Thus, finding a method to control the phase transition in a Josephson junction is still an urgent problem in condensed matter physics.

Recently, it has been proposed that a crossover from the suppressed to perfect Andreev reflection appears when the orientation of a normal metal–SC junction on the WSM surface with a pair of FAs is varied [40]. In other words, the transport properties can be changed by varying the orientation of the heterojunction. Therefore, it is interesting and necessary to investigate the relation between the supercurrent and the junction orientation in a Josephson junction. In this paper, the

*Contact author: yxli@mail.hebtu.edu.cn

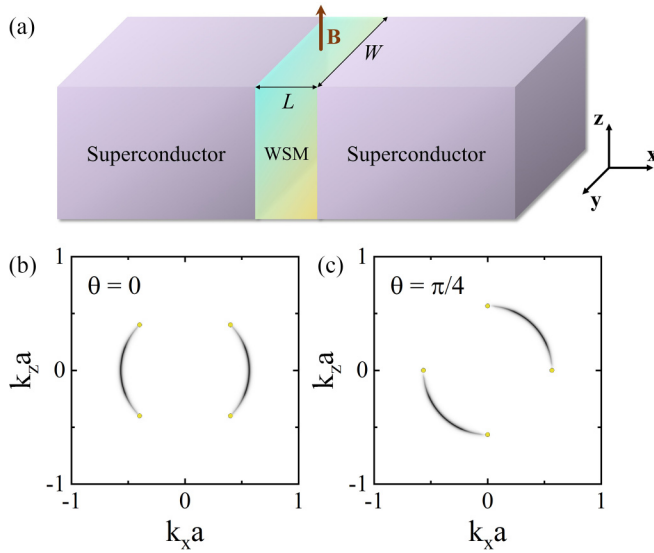


FIG. 1. (a) Schematic diagram of the superconductor (SC)–Weyl semimetal (WSM)–SC device. The center region is the WSM with length L and width W and subjected to an external magnetic field $\mathbf{B} = B\hat{z}$. The left and right leads are semi-infinite s -wave SCs. (b) and (c) Fermi-arc spectra for different azimuthal angles θ . The yellow dots represent Weyl points, whose positions are given by $U_y(\theta)\mathbf{k}_W = U_y(\theta)(\pm k, 0, \pm k)$.

supercurrent of the SC-WSM-SC Josephson junction hybrid system is studied based on the Landauer-Büttiker formula combined with the nonequilibrium Green's method. We calculate the supercurrent as functions of the magnetic field, the superconducting phase difference, and the azimuthal angle θ between the symmetry axis of the FAs and the normal of the Josephson junction, respectively. According to the different edge states, the FAs are divided into three regions, which are defined by the azimuthal angle θ and the transverse momentum k_z . The results show that the supercurrent behaves differently in these three regions, and the azimuthal angle θ can control the value of the supercurrent. In addition, the magnetic field and the azimuthal angle θ can adjust the phase transition of the Josephson junction, allowing it to be a 0 , π , or φ_0 junction.

The rest of the paper is organized as follows. In Sec. II, we introduce the Hamiltonian and energy band of WSM with a pair of FAs, along with the formulas and methods used to calculate the current through the superconducting leads. The numerical results are discussed in Sec. III. Finally, a brief summary is drawn in Sec. IV.

II. MODEL AND METHODS

We consider a SC-WSM-SC Josephson junction as shown in Fig. 1(a). The finite width along the y direction of the junctions is W . The length of WSM in the center region is L . The semi-infinite SC leads are placed in the left and right regions, respectively. The Hamiltonian of this hybrid device is written as

$$H = H_W + H_S + H_T, \quad (1)$$

where H_W , H_S , and H_T are the Hamiltonians of the WSM, SC leads, and the coupling between them, respectively.

In the tight-binding representation, the Hamiltonian of the WSM with four Weyl points can be written as [41]

$$H_W^0(\mathbf{k}) = M(k^2 - k_x^2)\sigma_x + M(k^2 - k_y^2 - k_z^2)\sigma_z + v_y k_y \sigma_y, \quad (2)$$

where v_y is the velocity in the y direction, k and M are parameters, and $\sigma_{x,y,z}$ are the Pauli matrices in the pseudospin space. The positions of the four Weyl points are $\mathbf{k}_W = (\pm k, 0, \pm k)$. The azimuthal angle between the symmetry axis of the FAs and the normal of the Josephson junction (x axis) is defined as θ , as shown in Fig. 2(a). The FAs rotate θ along the y axis corresponding to the Hamiltonian:

$$H_W^e(\mathbf{k}) = H_W^0[U_y(\theta)\mathbf{k}], \quad (3)$$

where

$$U_y(\theta) = \begin{pmatrix} \cos \theta & 0 & -\sin \theta \\ 0 & 1 & 0 \\ \sin \theta & 0 & \cos \theta \end{pmatrix}$$

is the rotation operator [42]. Experimentally, different orientations of FAs can be obtained by cutting the sample properly [41]. The FAs for different azimuthal angles θ are shown in Figs. 1(b) and 1(c), which are revealed by the spectra function $\mathcal{A}(E) = -(1/\pi)\text{Im}G^r(E)$ [40]. Using the Bogoliubov–de Gennes (BdG) equation to introduce holes [43], the Hamiltonian of the WSM becomes

$$H_W(\mathbf{k}) = \begin{bmatrix} H_W^e(\mathbf{k}) & 0 \\ 0 & H_W^h(\mathbf{k}) \end{bmatrix}, \quad (4)$$

where $H_W^h(\mathbf{k}) = -H_W^e*(-\mathbf{k})$. For a fixed k_z , we discretize the Hamiltonian of Eq. (4) in a cubic lattice through the mapping $k_{i=x,y,z} \rightarrow a^{-1}\sin k_i a$ and $k_i^2 \rightarrow 2a^{-2}(1 - \cos k_i a)$, where a is the lattice constant. Performing Fourier transformation in both the x and y directions, the Hamiltonian H_W in Eq. (1) is represented in the Nambu representation as

$$\begin{aligned} H_W = & \sum_{\mathbf{i}} \psi_{\mathbf{i}}^\dagger \begin{pmatrix} T_0 & 0 \\ 0 & -T_0 \end{pmatrix} \psi_{\mathbf{i}} + \sum_{\mathbf{i}} \psi_{\mathbf{i}}^\dagger \begin{pmatrix} T_y & 0 \\ 0 & -T_y \end{pmatrix} \psi_{\mathbf{i}+\hat{y}} \\ & + \sum_{\mathbf{i}} \psi_{\mathbf{i}}^\dagger \begin{bmatrix} T_x \exp(i\phi \frac{y}{a}) & 0 \\ 0 & -T_x \exp(-i\phi \frac{y}{a}) \end{bmatrix} \psi_{\mathbf{i}+\hat{x}} \\ & + \text{H.c.}, \end{aligned} \quad (5)$$

where $\psi_{\mathbf{i}} = (\psi_{1,\mathbf{i}\uparrow}, \psi_{2,\mathbf{i}\uparrow}, \psi_{1,\mathbf{i}\downarrow}^\dagger, \psi_{2,\mathbf{i}\downarrow}^\dagger)^T$ are the Fermi operators with two pseudospin components at the discrete site \mathbf{i} , \hat{x} and \hat{y} represent unit vectors in the x and y directions, respectively. Considering external magnetic field, $\phi = \Phi/\Phi_0$ is the magnetic field phase, $\Phi = Ba^2$ is the flux per plaquette, $\Phi_0 = \hbar c/e$ is the normal flux quantum, and $\mathbf{A} = (By, 0, 0)$ is the vector potential. The on-site and nearest-neighbor

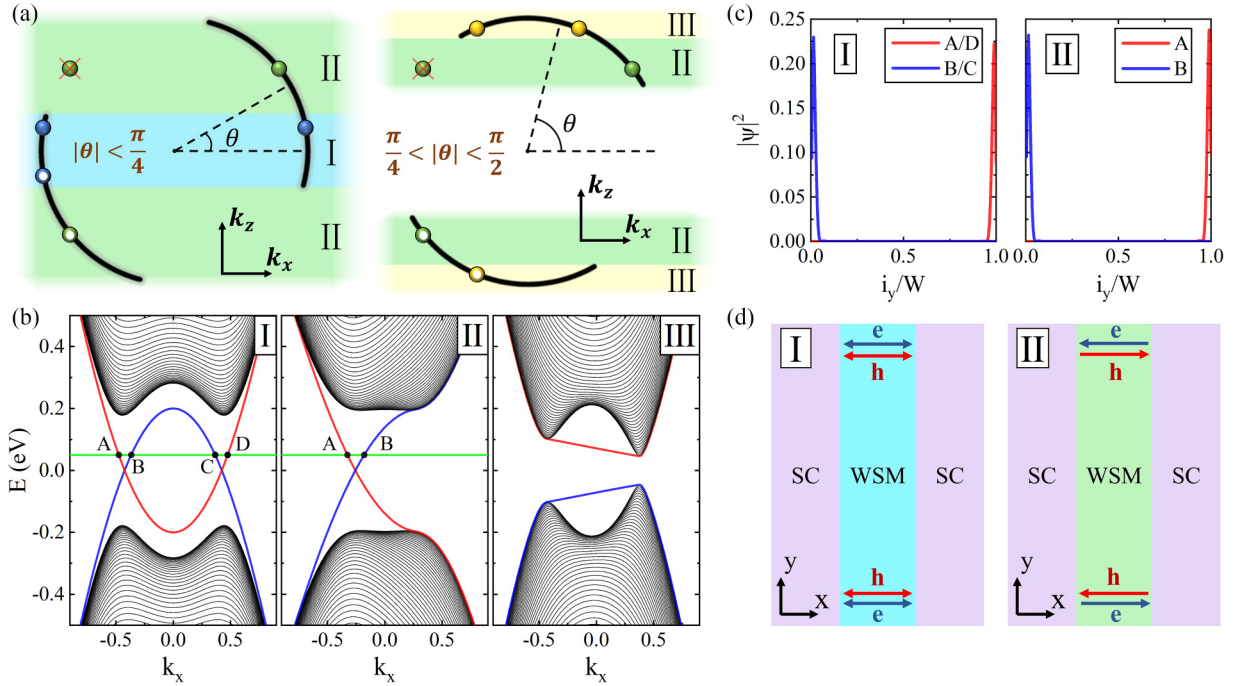


FIG. 2. (a) Schematic diagram for Fermi arcs of Weyl semimetal (WSM). Electrons and holes are solid and hollow circles, respectively. Regions I–III are defined by the azimuthal angle θ and the transverse momentum k_z . (b) Electron energy band structures for a fixed k_z in different regions. The red and blue solid lines are the electron edge states. (c) Distribution of electron states along the sample cross section in regions I and II, where A–D correspond to the points in (b). (d) Schematic diagram for Josephson junction in regions I and II. The blue and red arrows represent the electron and hole edge states of the WSM in the center region, respectively.

hopping matrices are

$$\begin{aligned}
 T_0 &= M \left[k^2 - \frac{2}{a^2} + \frac{2}{a^2} \sin^2 \theta \cos(k_z a) \right] \sigma_x \\
 &\quad + M \left[k^2 - \frac{4}{a^2} + \frac{2}{a^2} \cos^2 \theta \cos(k_z a) \right] \sigma_z, \\
 T_x &= M \left[\frac{1}{a^2} \cos^2 \theta - \frac{i}{a^2} \sin \theta \cos \theta \sin(k_z a) \right] \sigma_x \\
 &\quad + M \left[\frac{1}{a^2} \sin^2 \theta + \frac{i}{a^2} \sin \theta \cos \theta \sin(k_z a) \right] \sigma_z, \\
 T_y &= \frac{v_y}{2ai} \sigma_y + \frac{M}{a^2} \sigma_z.
 \end{aligned} \tag{6}$$

The schematic diagram for FAs of WSM, the electron band structure under zero magnetic field, and the electron state distribution along the sample cross-section are given in Fig. 2. From Figs. 2(a) and 2(b), we can see that the FAs are divided into three regions depending on the edge state, which are defined by the azimuthal angle θ and the transverse momentum k_z . In region I, both electrons and holes have bidirectional edge states [see Figs. 2(c) and 2(d)], that is, both normal reflection and Andreev reflection channels exist. Due to its symmetric Fermi-arc edge states, we refer to it as the symmetric region. In region II, which we designate as the topological region, electrons and holes have only one chiral edge state each, and their edge states are opposite [see Figs. 2(c) and 2(d)]. Consequently, the channel for normal electron reflection disappears, and the hole channel persists for Andreev reflection, which corresponds to the

electron-paired state with opposite k_z . In region III, the right panel of Fig. 2(a), WSM opens an energy gap at the Fermi level, leading to the absence of states near $E = 0$, so we refer to it as the insulated region. It is worth noting that k_z is fixed, which is treated as a parameter in the scattering process. If we only consider a single 2D slice with a given k_z , which is a subsystem of the entire three-dimensional (3D) WSM, the band structure breaks the particle-hole symmetry. By summing all k_z channels, the particle-hole symmetry is preserved [40].

Then according to the BCS theory [44], the Hamiltonian of the SC lead described by a continuum model can be written as

$$H_S = \sum_{\alpha, \mathbf{k}, \sigma} \epsilon_{\alpha \mathbf{k}} b_{\alpha \mathbf{k} \sigma}^\dagger b_{\alpha \mathbf{k} \sigma} + \sum_{\alpha, \mathbf{k}} (\Delta b_{\alpha \mathbf{k} \uparrow}^\dagger b_{\alpha -\mathbf{k} \downarrow}^\dagger + \text{H.c.}), \tag{7}$$

where α refers to the left or right lead and σ represents the spin index. Here, $\Delta = \Delta_s \exp(i\varphi_\alpha)$, where Δ_s is the superconducting gap magnitude of the s -wave SC and φ_α is the superconducting phase. Also, $b_{\alpha \mathbf{k} \sigma}^\dagger$ ($b_{\alpha \mathbf{k} \sigma}$) is the creation (annihilation) operator in the SC leads for electrons with the momentum $\mathbf{k} = (k_x, k_y)$. The coupling between the SC lead and the WSM is described by the Hamiltonian:

$$H_T = \sum_{\alpha, i_y} (b_{\alpha i_y \uparrow}^\dagger, b_{\alpha i_y \downarrow}) T_{\alpha c} \psi_{i_y} + \text{H.c.}, \tag{8}$$

where the operator:

$$b_{\alpha i_y \sigma} = \sum_{\mathbf{k}} \exp(i\mathbf{k} i_y a) b_{\alpha \mathbf{k} \sigma},$$

and

$$T_{\alpha c} = \begin{pmatrix} t_{\alpha c}^1 & t_{\alpha c}^2 & 0 & 0 \\ 0 & 0 & -t_{\alpha c}^1 & -t_{\alpha c}^2 \end{pmatrix}.$$

The parameters $t_{\alpha c}^1$ and $t_{\alpha c}^2$ are the coupling strengths between the SCs and the WSM.

Next, based on the Landauer-Büttiker formula combined with the nonequilibrium Green's function method, the supercurrent from the left lead through the center region to the right lead can be obtained as [45,46]

$$I_S = \frac{e}{h} \int dE \text{Tr} [\Gamma_z G^r(E) \Sigma_\alpha^<(E) + \Gamma_z G^<(E) \Sigma_\alpha^a(E) - \Gamma_z \Sigma_\alpha^<(E) G^a(E) - \Gamma_z \Sigma_\alpha^r(E) G^<(E)], \quad (9)$$

where E is the incident energy and $\Gamma_z = \sigma_z \otimes I_{2 \times 2}$. Here, $G^{r,a,<}$ are the retarded, advanced, and lesser Green's functions of the center region which can be calculated from [45–47]

$$G^{r/a}(E) = (EI - H_{\text{cen}} - \Sigma_L^{r/a} - \Sigma_R^{r/a} \pm i\gamma)^{-1},$$

$$G^< = G^r \Sigma^< G^a = G^r (\Sigma_L^< + \Sigma_R^<) G^a, \quad (10)$$

where H_{cen} is the Hamiltonian of the central WSM region and γ is the linewidth function of states. Here, $\Sigma_\alpha^{r,a,<}$ are the retarded, advanced, and lesser self-energy due to the coupling between the α lead and the center region which can be calculated from [47]

$$\Sigma_{\alpha,ij}^r(E) = -i\pi\rho|t_c|^2 J_0[k_F(y_i - y_j)] \beta(E) \begin{pmatrix} 1 & \Delta/E \\ \Delta^*/E & 1 \end{pmatrix}$$

$$= -\frac{i}{2} \Gamma_{\alpha,ij}(E),$$

$$\Sigma_{\alpha,ij}^a(E) = \frac{i}{2} \Gamma_{\alpha,ij}^*(E),$$

$$\Sigma_{\alpha,ij}^<(E) = -f(E) (\Sigma_{\alpha,ij}^r - \Sigma_{\alpha,ij}^a), \quad (11)$$

where $f(E)$ is the Fermi distribution function and t_c represents $t_{\alpha c}^1$ or $t_{\alpha c}^2$. To simplify the model, we set $t_{\alpha c}^1 = t_{\alpha c}^2 = t_c$, and the final self-energy takes the form $\Sigma_\alpha \otimes I_{2 \times 2}$.

In this paper, we set the parameters $k = 0.4 \text{ nm}^{-1}$ and $M = 1.25 \text{ eV nm}^2$, the velocity in the y direction $v_y = -0.66 \text{ eV nm}$, and the lattice constant $a = 1 \text{ nm}$. The length and width of the central WSM region are $L = 20a$ and $W = 40a$, respectively. The superconducting gap magnitude $\Delta_s = 0.01 \text{ eV}$, the superconducting phase difference $\Delta\phi = \phi_L - \phi_R$, and the coupling coefficient $t_c = 1 \text{ eV}$. The linewidth γ is usually chosen as an infinitely small quantity in a clean sample. Since the finite width of the central sample adopted in our simulation results in discrete energy levels, a relatively large γ is required to smear the discrete energy levels and makes them look like a continuous energy spectrum. In addition, the disorder present in the real sample may lead to broadening of states [45]. Therefore, we chose a relatively large linewidth $\gamma = 0.05 \text{ eV}$ in this paper. In addition, it is worth noting that, once we determine the transport direction x and the good quantum number k_z , the FA surface states can only exist in the x - z plane to control the supercurrent. However, the FA surface states in other planes have little effect on the supercurrent.

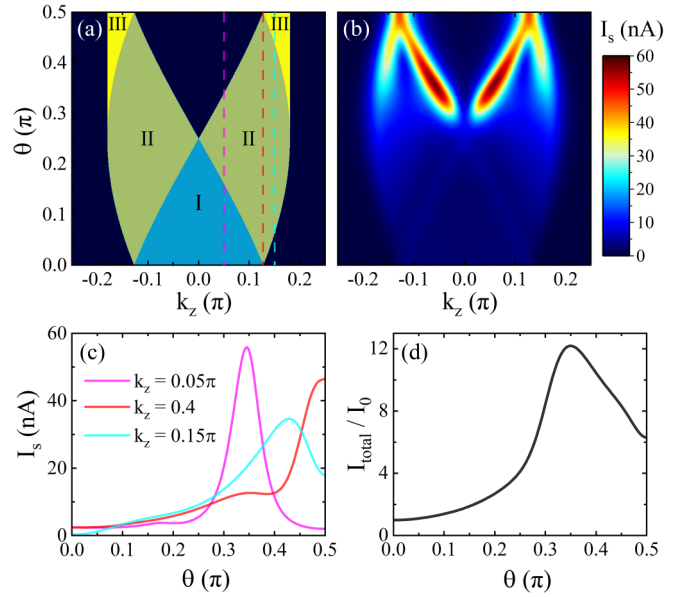


FIG. 3. (a) Distribution diagram for different regions of Fermi arcs that vary with azimuthal angle θ and momentum k_z at the zero magnetic field. The pink, red, and cyan dashed lines represent the channels at $k_z = 0.05\pi$, 0.4 , and 0.15π , respectively. (b) Supercurrent I_s in a two-dimensional (2D) slice as a function of azimuthal angle θ and momentum k_z without the magnetic field. The superconducting phase difference $\Delta\phi = \frac{\pi}{2}$. (c) Supercurrent I_s for the different k_z channels in (b) which corresponds to the dashed lines in (a). (d) The total supercurrent I_{total} for the sum of all k_z channels in (b) as a function of azimuthal angle θ , where I_0 is the total supercurrent of all channels at $\theta = 0$, $\phi = 0$, and $\Delta\phi = \frac{\pi}{2}$.

III. RESULTS AND DISCUSSION

First, we study the supercurrent in the absence of a magnetic field. To elucidate more clearly, we plotted the distribution diagram for different regions of Fermi arcs that vary with azimuthal angle θ and momentum k_z , as shown in Fig. 3(a). It is observable that the symmetric region presents a triangular shape, the topological region is the largest and presents two opposing fan shapes, the insulated region is the smallest and located at the edge of the topological region, and the rest of the dark blue area is referred to as the blank region. At $\theta = 0$, only the symmetric region exists with the range $k_z \in [-0.4, 0.4]$, which is related to the positions of the Weyl points. As θ increases, the topological region begins to emerge at $|k_z| = 0.4$ and gradually widens; the symmetric region correspondingly decreases. When θ increases to $\pi/4$, only the topological region exists. As θ continues to increase beyond $\pi/4$, the topological region begins to decrease, and the insulated region begins to appear. When θ increases to $\pi/2$, only the insulated region remains.

Then we calculate the supercurrent as a function of the azimuthal angle θ and momentum k_z ; the results are shown in Fig. 3(b). Compared with Fig. 3(a), the supercurrent exists in both the symmetric and topological regions, but almost none exists in the insulated region. Moreover, the supercurrent is obviously larger in the topological region than in the symmetric region and increases as θ increases. These phenomena

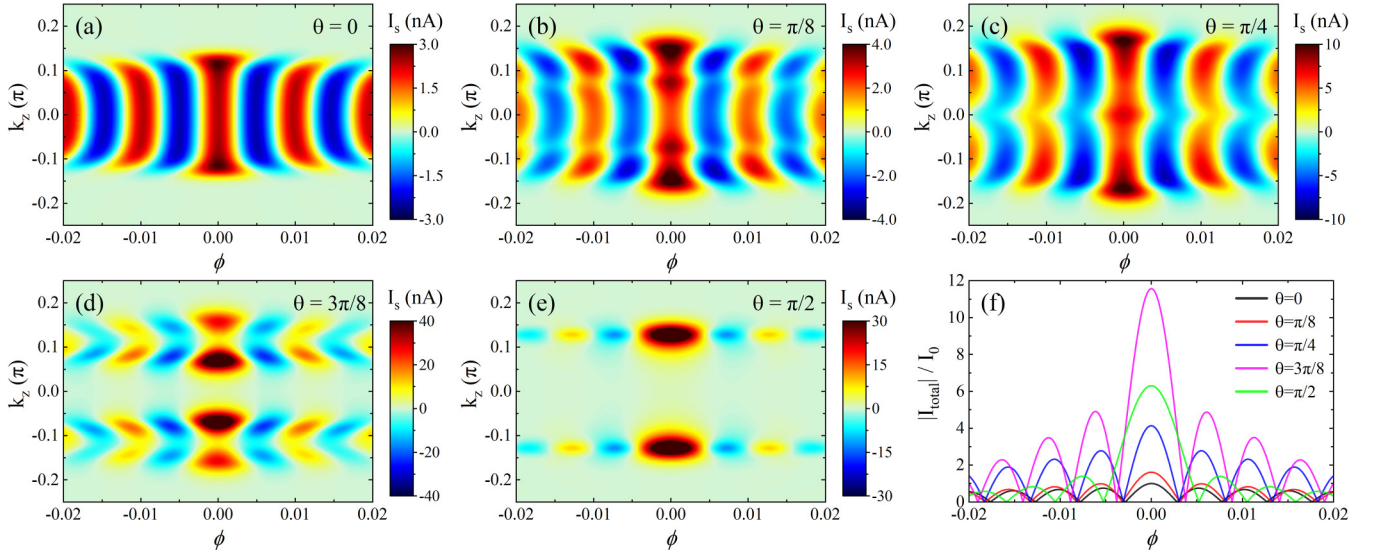


FIG. 4. (a)–(e) Supercurrent I_s in a two-dimensional (2D) slice as a function of momentum k_z and magnetic field phase ϕ for the different azimuthal angles θ . The superconducting phase difference $\Delta\varphi = \frac{\pi}{2}$ and $\theta = 0, \frac{\pi}{8}, \frac{\pi}{4}, \frac{3\pi}{8}, \frac{\pi}{2}$, respectively. (f) The absolute value of the total supercurrent I_{total} for the sum of all k_z channels in (a)–(e) as a function of magnetic field phase ϕ , where I_0 is the total supercurrent of all channels at $\theta = 0, \phi = 0$, and $\Delta\varphi = \frac{\pi}{2}$.

can be explained by the band structure as shown in Fig. 2. In the symmetric region, since both electrons and holes have bidirectional edge states, that is, both normal reflection and Andreev reflection channels exist, this reduces the occurrence of Andreev reflection at the SC-WSM interface, thereby reducing the supercurrent. In contrast, in the topological region, electrons and holes have only one chiral edge state, meaning that only the hole channel for Andreev reflection exists. In this case, the perfect Andreev reflection occurs [40], allowing the electrons in the center region to effectively participate in the supercurrent transport, thereby increasing the supercurrent.

Figure 3(c) selects three specific channels for further illustration. Firstly, let us consider the channel of $k_z = 0.4$, which remains within the topological region regardless of the value of θ . It can be seen from the Supplemental Material [48] that the slope of the edge states gradually decreases to zero with increasing θ , resulting in an increase of states in the interval from E to $E + dE$; thus, the supercurrent increases, and the growth trend is approximately proportional to the reciprocal of the edge state slope. In other channels within the topological region, the supercurrent increases with θ for the same reason. For the channel of $k_z = 0.05\pi$, as θ increases, it first resides in the symmetric region, where the supercurrent growth is relatively gentle. Then it enters the topological region, where the supercurrent rapidly increases and reaches a peak. Finally, as θ continues to increase outside the topological region, the supercurrent rapidly decreases. For the channel of $k_z = 0.15\pi$, it is initially in the blank region, so the supercurrent approaches zero. The current begins to increase rapidly as it enters the topological region and begins to decrease as it enters the insulated region. At $\theta = \pi/2$, it is in the insulated region, but the supercurrent does not approach zero. The Supplemental Material [48] shows that, at $\theta = \pi/2$

and $k_z = 0.4$, the energy gap is very small. Therefore, the bands near this set of parameters have smaller gaps, and the larger linewidth smears the energy levels, resulting in the presence of the supercurrent.

Then we sum the supercurrent of all k_z channels in Fig. 3(d). As θ increases, the total supercurrent I_{total} first increases and then decreases. This is because, when θ begins to increase, the topological region with enhanced supercurrent starts to appear and keeps increasing, the symmetric region with suppressed supercurrent keeps decreasing, and the supercurrent in the topological region increases as θ increases. This causes I_{total} to increase continuously and begin to increase rapidly near $\theta = \pi/4$. When θ increases beyond $\pi/4$, although the supercurrent in the topological region is still increasing, the number of channels in this region begins to decrease, eventually causing I_{total} to decrease around $\theta = 0.35\pi$. Lastly, due to the smaller energy gaps and larger linewidth, the total supercurrent reaches a finite value when $\theta = \pi/2$.

Next, we study the effect of the magnetic field on the supercurrent. Figures 4(a)–4(e) show the supercurrent in a 2D slice as a function of momentum k_z and magnetic field phase ϕ for the different azimuthal angles θ . Significantly, the supercurrent exhibits a characteristic like the single-slit Fraunhofer interference pattern as the magnetic field changes. When $\theta = 0$, all k_z channels with supercurrent are in the symmetric region [see Fig. 4(a)]. As $|k_z|$ increases, the oscillation period increases. Moreover, the height difference between the main peak and the subpeaks is not significant, and the peaks decrease sequentially with the magnetic field increasing. As θ increases, the topological region starts to appear at channels with $|k_z| = 0.4$ and gradually widens; the range of the symmetric region correspondingly decreases [see Figs. 4(b) and 4(c)]. Overall, the number of channels with supercurrent

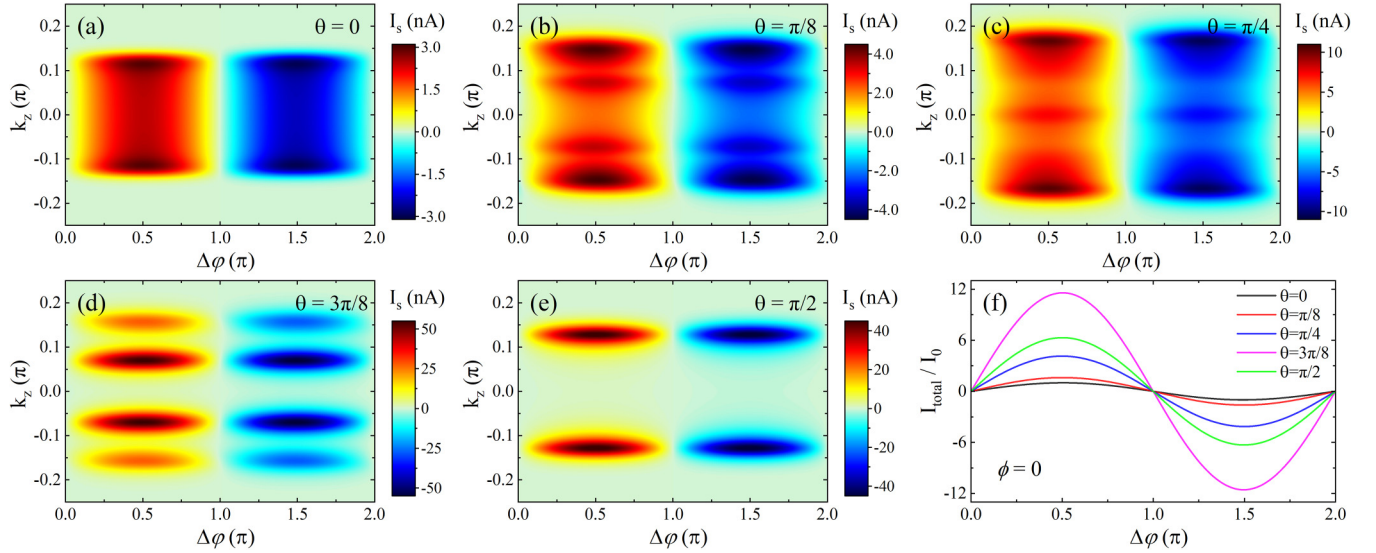


FIG. 5. (a)–(e) Supercurrent I_s in a two-dimensional (2D) slice as a function of momentum k_z and superconducting phase difference $\Delta\phi$ for the different azimuthal angles θ without the magnetic field. The magnetic field phase $\phi = 0$ and $\theta = 0, \frac{\pi}{8}, \frac{\pi}{4}, \frac{3\pi}{8}, \frac{\pi}{2}$, respectively. (f) The total supercurrent I_{total} for the sum of all k_z channels in (a)–(e) as a function of superconducting phase difference $\Delta\phi$, where I_0 is the total supercurrent of all channels at $\theta = 0, \phi = 0$, and $\Delta\phi = \frac{\pi}{2}$.

gradually increases. When θ increases to $\pi/4$, only the topological region exists. Due to the perfect Andreev reflection in the topological region, the supercurrent is significantly larger than that in the symmetric region. Unlike in the symmetric region, its main peak is much higher than the subpeaks, and the period first decreases and then increases as $|k_z|$ increases. As θ increases beyond $\pi/4$, the topological region begins to narrow and break at $k_z = 0$, at which point the period changes more significantly with k_z [see Fig. 4(d)]. Next, as θ increases to $\pi/2$, the supercurrent does not decrease to zero and exists

in two narrow regions around $|k_z| = 0.4$, which is consistent with previous analysis. Finally, we sum the supercurrent of all the k_z channels, as shown in Fig. 4(f). The results show that, as θ increases, the total supercurrent first increases and then decreases, the oscillation period and the height difference between the main and subpeaks increase.

Then we study the relationship between supercurrent and superconducting phase difference. Figures 5(a)–5(e) show the supercurrent in a 2D slice as a function of momentum k_z and superconducting phase difference $\Delta\phi$ without the magnetic

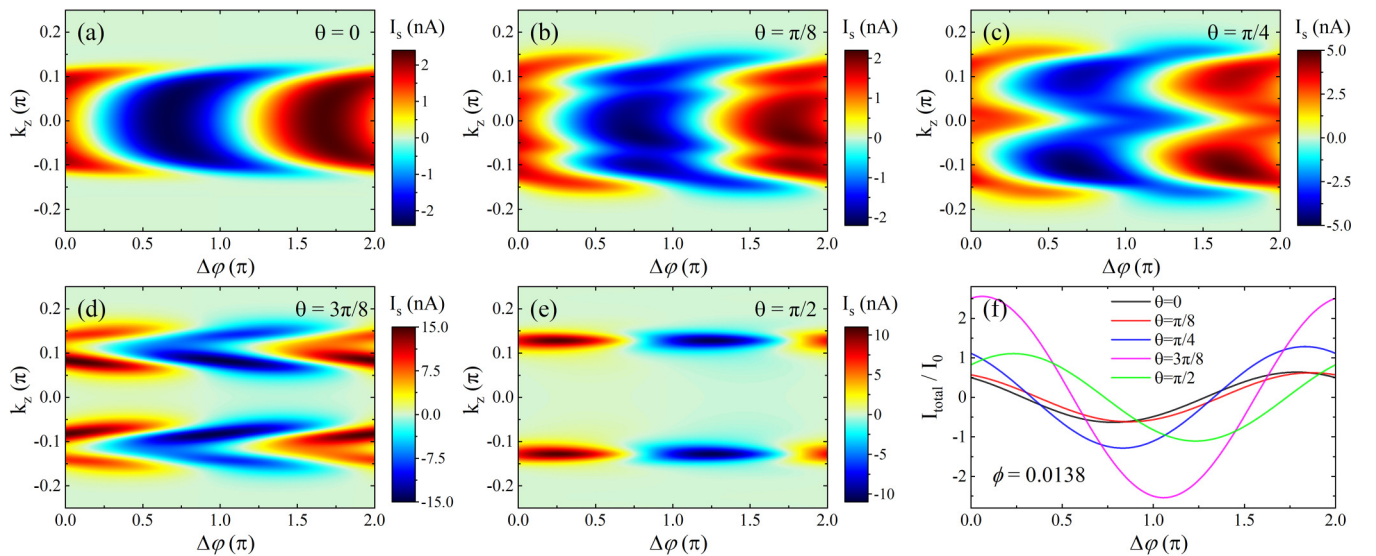


FIG. 6. (a)–(e) Supercurrent I_s in a two-dimensional (2D) slice as a function of momentum k_z and superconducting phase difference $\Delta\phi$ for the different azimuthal angles θ with the magnetic field. The magnetic field phase $\phi = 0.0138$ and $\theta = 0, \frac{\pi}{8}, \frac{\pi}{4}, \frac{3\pi}{8}, \frac{\pi}{2}$, respectively. (f) The total supercurrent I_{total} for the sum of all k_z channels in (a)–(e) as a function of superconducting phase difference $\Delta\phi$, where I_0 is the total supercurrent of all channels at $\theta = 0, \phi = 0$, and $\Delta\phi = \frac{\pi}{2}$.

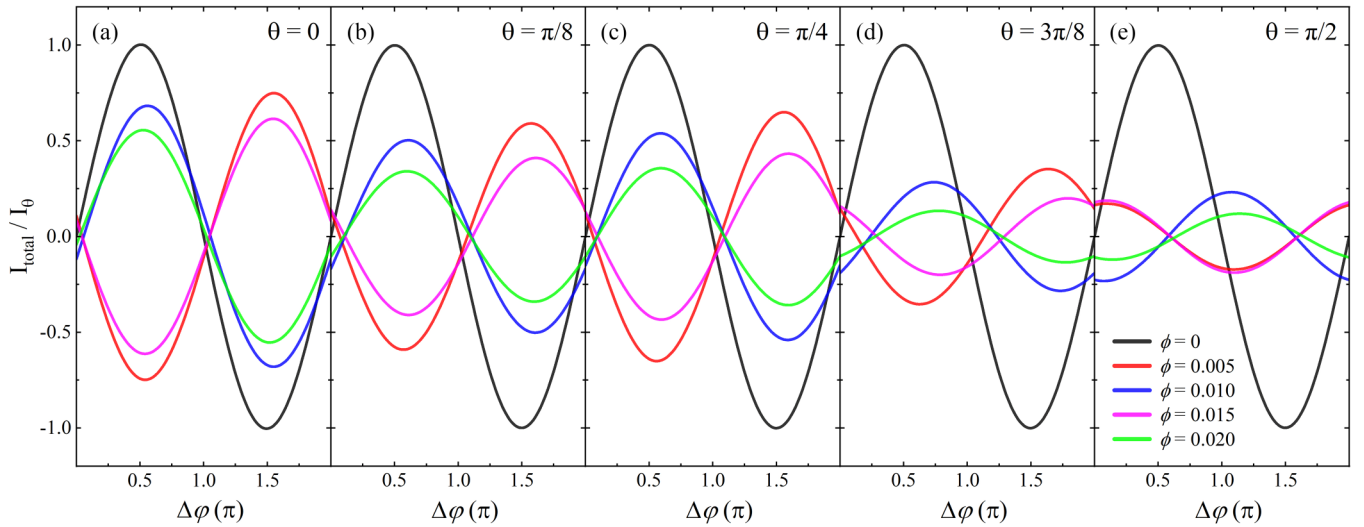


FIG. 7. The total supercurrent I_{total} for the sum of all k_z channels as a function of superconducting phase difference $\Delta\varphi$ for the different magnetic field phases ϕ , where I_θ is the total supercurrent of all channels at $\phi = 0$, $\Delta\varphi = \frac{\pi}{2}$, and $\theta = 0, \frac{\pi}{8}, \frac{\pi}{4}, \frac{3\pi}{8}, \frac{\pi}{2}$ in (a)–(e), respectively.

field. In all k_z channels, regardless of the value of θ , the supercurrent varies with $\Delta\varphi$ as a sine function of period 2π , that is, $I_s(k_z, \theta) = I_c \sin(\Delta\varphi + \Delta\varphi_0)$, where I_c is the critical current and $\Delta\varphi_0$ is the additional phase. Since $\Delta\varphi_0 = 0$ for all k_z channels, the total supercurrent shown in Fig. 5(f) as a function of $\Delta\varphi$ satisfies the sine function with period 2π and the zero additional phase. That is, under zero magnetic field, the Josephson junction is a 0 junction regardless of the value of θ . In addition, the variation patterns of the supercurrent with θ in three regions are consistent with previous analyses, so the critical current of the total supercurrent also increases first and then decreases with θ increasing.

Next, we arbitrarily choose a magnetic field phase ($\phi = 0.0138$) to discuss the presence of a magnetic field. We can see from Fig. 6 that, under the influence of a magnetic field, the relationship between the supercurrent and the superconducting phase difference $\Delta\varphi$ still follows a sine function with a period of 2π , but the additional phase $\Delta\varphi_0$ is no longer zero. When $\theta = 0$, all k_z channels are in the symmetric region, $\Delta\varphi_0$ decreases with increasing $|k_z|$ [see Fig. 6(a)]. As θ increases, the topological region begins to appear. Unlike the symmetric region, $\Delta\varphi_0$ first increases and then decreases as $|k_z|$ increases in the topological region [see Figs. 6(b)–6(d)]. Obviously, the magnitude of the supercurrent is similar in the symmetric and topological regions, which is related to the decrease of the values of the subpeaks due to the increase of the magnetic field. In Fig. 4(f), we can see that, when $\phi = 0.0138$, the values of supercurrent corresponding to different θ 's are close. As θ increases to $\pi/2$, only the insulated region remains, and $\Delta\varphi_0$ no longer changes significantly with $|k_z|$ [see Fig. 6(e)]. Since the k_z channels corresponding to different θ 's have different $\Delta\varphi_0$'s, the total supercurrents corresponding to different θ 's also have different additional phases. That is, under the influence of the magnetic field, the Josephson junction transforms into a φ_0 junction, and the additional phase can be adjusted by changing θ [see Fig. 6(f)].

Lastly, in the experiment, only the total supercurrent from all k_z channels can be observed, and the magnetic field and

superconducting phase difference are easier to adjust than the azimuthal angle θ . Therefore, we plot the total supercurrent I_{total} as a function of superconducting phase difference $\Delta\varphi$ for the different magnetic field phases ϕ , as shown in Fig. 7. When the magnetic field is zero, the Josephson junction is a 0 junction regardless of the value of θ . As the magnetic field phase increases, the 0- π transition appears in the supercurrent, and the 0 and π junctions alternately appear [see Fig. 7(a)]. In addition, as θ increases, the additional phase of both the 0 and π junctions increases, resulting in the Josephson junction transforming into a φ_0 junction. The additional phase can be increased to more than $\pi/2$ [see Fig. 7(e)]. This means that the magnetic field and the azimuthal angle θ can adjust the phase transition of the Josephson junction, allowing it to be a 0, π , or φ_0 junction.

IV. CONCLUSIONS

In summary, we have studied the supercurrent in the SC-WSM-SC junction. According to the different edge states, the FAs are divided into three regions. Different edge states possess distinct channels for normal reflection and Andreev reflection. This determines whether perfect Andreev reflection can occur at the SC-WSM interface, thus affecting whether electrons in the center region can effectively participate in supercurrent transport. It is found that the supercurrent is suppressed in the symmetric region. In the topological region, the supercurrent increases with increasing θ . The supercurrent is almost zero in the insulated region due to the presence of the energy gap. The total supercurrent increases and then decreases with increasing θ , that is, θ can control the value of the supercurrent. The Josephson junction is a 0 junction regardless of the value of θ without the magnetic field. In the presence of a magnetic field, the supercurrent exhibits a characteristic like the single-slit Fraunhofer interference pattern as the magnetic field varies. In this case, the magnetic field and the azimuthal angle θ can adjust the phase

transition of the Josephson junction, allowing it to be a 0, π , or φ_0 junction. These properties provide research ideas for controlling the value of supercurrent and the Josephson junction phase transition and play an important role in the development and application of superconducting electronic devices.

ACKNOWLEDGMENTS

This paper was supported by the National Natural Science Foundation of China (Grant No. 11874139) and the Natural Science Foundation of Hebei Province (Grant No. A2019205190).

-
- [1] F. D. Haldane, Model for a quantum Hall effect without Landau levels: Condensed-matter realization of the “parity anomaly”, *Phys. Rev. Lett.* **61**, 2015 (1988).
- [2] C. L. Kane and E. J. Mele, Z_2 topological order and the quantum spin Hall effect, *Phys. Rev. Lett.* **95**, 146802 (2005).
- [3] L. Fu, Topological crystalline insulators, *Phys. Rev. Lett.* **106**, 106802 (2011).
- [4] S. M. Young, S. Zaheer, J. C. Teo, C. L. Kane, E. J. Mele, and A. M. Rappe, Dirac semimetal in three dimensions, *Phys. Rev. Lett.* **108**, 140405 (2012).
- [5] L. P. He, X. C. Hong, J. K. Dong, J. Pan, Z. Zhang, J. Zhang, and S. Y. Li, Quantum transport evidence for the three-dimensional Dirac semimetal phase in Cd_3As_2 , *Phys. Rev. Lett.* **113**, 246402 (2014).
- [6] H. B. Nielsen and M. Ninomiya, The Adler-Bell-Jackiw anomaly and Weyl fermions in a crystal, *Phys. Lett. B* **130**, 389 (1983).
- [7] A. A. Burkov and L. Balents, Weyl semimetal in a topological insulator multilayer, *Phys. Rev. Lett.* **107**, 127205 (2011).
- [8] X. G. Wan, A. M. Turner, A. Vishwanath, and S. Y. Savrasov, Topological semimetal and Fermi-arc surface states in the electronic structure of pyrochlore iridates, *Phys. Rev. B* **83**, 205101 (2011).
- [9] A. A. Soluyanov, D. Gresch, Z. J. Wang, Q. S. Wu, M. Troyer, X. Dai, and B. A. Bernevig, Type-II Weyl semimetals, *Nature (London)* **527**, 495 (2015).
- [10] S. M. Huang, S. Y. Xu, I. Belopolski, C. C. Lee, G. Chang, B. K. Wang, N. Alidoust, G. Bian, M. Neupane, C. Zhang *et al.*, A Weyl fermion semimetal with surface Fermi arcs in the transition metal monopychlide TaAs class, *Nat. Commun.* **6**, 7373 (2015).
- [11] S.-Y. Xu, I. Belopolski, N. Alidoust, M. Neupane, G. Bian, C. Zhang, R. Sankar, G. Chang, Z. Yuan, C.-C. Lee *et al.*, Discovery of a Weyl fermion semimetal and topological Fermi arcs, *Science* **349**, 613 (2015).
- [12] J. Ruan, S.-K. Jian, D. Zhang, H. Yao, H. Zhang, S.-C. Zhang, and D. Xing, Ideal Weyl semimetals in the chalcopyrites CuTiSe_2 , AgTiTe_2 , AuTiTe_2 , and ZnPbAs_2 , *Phys. Rev. Lett.* **116**, 226801 (2016).
- [13] A. A. Burkov, M. D. Hook, and L. Balents, Topological nodal semimetals, *Phys. Rev. B* **84**, 235126 (2011).
- [14] C. Fang, H. M. Weng, X. Dai, and Z. Fang, Topological nodal line semimetals, *Chin. Phys. B* **25**, 117106 (2016).
- [15] H. B. Nielsen and M. Ninomiya, A no-go theorem for regularizing chiral fermions, *Phys. Lett. B* **105**, 219 (1981).
- [16] S.-Y. Xu, N. Alidoust, I. Belopolski, Z. Yuan, G. Bian, T.-R. Chang, H. Zheng, V. N. Strocov, D. S. Sanchez, G. Chang *et al.*, Discovery of a Weyl fermion state with Fermi arcs in niobium arsenide, *Nat. Phys.* **11**, 748 (2015).
- [17] N. Xu, H. Weng, B. Lv, C. E. Matt, J. Park, F. Bisti, V. N. Strocov, D. Gawryluk, E. Pomjakushina, K. Conder *et al.*, Observation of Weyl nodes and Fermi arcs in tantalum phosphide, *Nat. Commun.* **7**, 11006 (2016).
- [18] L. Yang, Z. Liu, Y. Sun, H. Peng, H. Yang, T. Zhang, B. Zhou, Y. Zhang, Y. Guo, M. Rahn *et al.*, Weyl semimetal phase in the non-centrosymmetric compound TaAs, *Nat. Phys.* **11**, 728 (2015).
- [19] L. Huang, T. M. McCormick, M. Ochi, Z. Zhao, M.-T. Suzuki, R. Arita, Y. Wu, D. Mou, H. Cao, J. Yan *et al.*, Spectroscopic evidence for a type II Weyl semimetallic state in MoTe_2 , *Nat. Mater.* **15**, 1155 (2016).
- [20] B. D. Josephson, Possible new effects in superconductive tunnelling, *Phys. Lett.* **1**, 251 (1962).
- [21] B. D. Josephson, The discovery of tunnelling supercurrents, *Rev. Mod. Phys.* **46**, 251 (1974).
- [22] P. W. Anderson and J. M. Rowell, Probable observation of the Josephson superconducting tunneling effect, *Phys. Rev. Lett.* **10**, 230 (1963).
- [23] A. F. Andreev, The thermal conductivity of the intermediate state in superconductors, *Sov. Phys. JETP* **19**, 1228 (1964).
- [24] C. W. J. Beenakker, Universal limit of critical-current fluctuations in mesoscopic Josephson junctions, *Phys. Rev. Lett.* **67**, 3836 (1991).
- [25] C. W. J. Beenakker, Quantum transport in semiconductor-superconductor microjunctions, *Phys. Rev. Lett.* **68**, 1442(E) (1992).
- [26] I. O. Kulik, Macroscopic quantization and the proximity effect in SNS junctions, *Sov. Phys. JETP* **30**, 944 (1970).
- [27] A. I. Buzdin, Proximity effects in superconductor-ferromagnet heterostructures, *Rev. Mod. Phys.* **77**, 935 (2005).
- [28] V. V. Ryazanov, V. A. Oboznov, A. Yu. Rusanov, A. V. Veretennikov, A. A. Golubov, and J. Aarts, Coupling of two superconductors through a ferromagnet: Evidence for a π junction, *Phys. Rev. Lett.* **86**, 2427 (2001).
- [29] M. Houzet and A. I. Buzdin, Long range triplet Josephson effect through a ferromagnetic trilayer, *Phys. Rev. B* **76**, 060504(R) (2007).
- [30] M. Eschrig and T. Löfwander, Triplet supercurrents in clean and disordered half-metallic ferromagnets, *Nat. Phys.* **4**, 138 (2008).
- [31] K. Halterman, O. T. Valls, and C.-T. Wu, Charge and spin currents in ferromagnetic Josephson junctions, *Phys. Rev. B* **92**, 174516 (2015).
- [32] J. A. Ouassou, A. Brataas, and J. Linder, dc Josephson effect in altermagnets, *Phys. Rev. Lett.* **131**, 076003 (2023).
- [33] T. Kontos, M. Aprili, J. Lesueur, and X. Grison, Inhomogeneous superconductivity induced in a ferromagnet by proximity effect, *Phys. Rev. Lett.* **86**, 304 (2001).

- [34] V. A. Oboznov, V. V. Bol'ginov, A. K. Feofanov, V. V. Ryazanov, and A. I. Buzdin, Thickness dependence of the Josephson ground states of superconductor-ferromagnet-superconductor junctions, *Phys. Rev. Lett.* **96**, 197003 (2006).
- [35] A. Buzdin, Direct coupling between magnetism and superconducting current in the Josephson φ_0 junction, *Phys. Rev. Lett.* **101**, 107005 (2008).
- [36] T. Yokoyama, M. Eto, and Y. V. Nazarov, Anomalous Josephson effect induced by spin-orbit interaction and Zeeman effect in semiconductor nanowires, *Phys. Rev. B* **89**, 195407 (2014).
- [37] K. N. Nesterov, M. Houzet, and J. S. Meyer, Anomalous Josephson effect in semiconducting nanowires as a signature of the topologically nontrivial phase, *Phys. Rev. B* **93**, 174502 (2016).
- [38] V. Braude and Y. V. Nazarov, Fully developed triplet proximity effect, *Phys. Rev. Lett.* **98**, 077003 (2007).
- [39] M. Alidoust and H. Hamzeshpour, Spontaneous supercurrent and φ_0 phase shift parallel to magnetized topological insulator interfaces, *Phys. Rev. B* **96**, 165422 (2017).
- [40] Y. Zheng, W. Chen, and D. Y. Xing, Andreev reflection in Fermi-arc surface states of Weyl semimetals, *Phys. Rev. B* **104**, 075420 (2021).
- [41] G. Chen, O. Zilberberg, and W. Chen, Detection of Fermi arcs in Weyl semimetals through surface negative refraction, *Phys. Rev. B* **101**, 125407 (2020).
- [42] W. Chen, L. Jiang, R. Shen, L. Sheng, B. Wang, and D. Xing, Specular Andreev reflection in inversion-symmetric Weyl semimetals, *Europhys. Lett.* **103**, 27006 (2013).
- [43] P. G. De Gennes, *Superconductivity of Metals and Alloys* (Benjamin, New York, 1966).
- [44] J. Bardeen, L. N. Cooper, and J. R. Schrieffer, Microscopic theory of superconductivity, *Phys. Rev.* **106**, 162 (1957).
- [45] J. Song, H. Liu, J. Liu, Y.-X. Li, R. Joynt, Q.-F. Sun, and X. C. Xie, Quantum interference in topological insulator Josephson junctions, *Phys. Rev. B* **93**, 195302 (2016).
- [46] J. Liu, H. Liu, J. Song, Q.-F. Sun, and X. C. Xie, Superconductor-graphene-superconductor Josephson junction in the quantum Hall regime, *Phys. Rev. B* **96**, 045401 (2017).
- [47] Q.-F. Sun and X. C. Xie, Quantum transport through a graphene nanoribbon-superconductor junction, *J. Phys.: Condens. Matter* **21**, 344204 (2009).
- [48] See Supplemental Material at <http://link.aps.org/supplemental/10.1103/PhysRevB.109.235435> for dynamic diagram of the band structure of a specific 2D slice of the WSM with a pair of Fermi arcs varying with the azimuthal angle between the symmetry axis of the Fermi arcs and the normal of the Josephson junction.